

# Application of Ag/ZnO composite materials in nitrogen photofixation: Constructing Schottky barrier to realized effective charge carrier separation

XIAO Yu, OUYANG Yu-xin, XIN Yue, WANG Liang-bing\*

(State Key Laboratory for Powder Metallurgy, School of Materials Science and Engineering,  
Central South University, Changsha 410083, China)

**Abstract:** The photocatalytic reduction of nitrogen ( $N_2$ ) to ammonia ( $NH_3$ ) is a sustainable energy product method. Plasmonic photocatalysts can achieve effective conversion of solar energy via surface plasmon resonance (SPR), and therefore have attracted more and more attention. However, the photo-induced hot charge-carriers tend to recombine during  $N_2$  reduction process. Ag nanoparticles with plasmon resonance effect with ZnO semiconductor (Ag/ZnO) and apply them to  $N_2$  photofixation were studied. Compared with pure ZnO, Ag/ZnO exhibited enhanced catalytic activity in  $N_2$  photofixation, and the  $NH_3$  production rate at room temperature can reach  $120 \mu\text{mol} \cdot \text{g}_{\text{cat}}^{-1} \cdot \text{h}^{-1}$ . Mechanism studies revealed that a Schottky barrier was formed at the interface between Ag nanoparticles and ZnO, which boosted the separation of photo-induced electron-hole pairs. Ag nanoparticles generated hot charge carriers via SPR effect, and the formed Schottky barrier facilitated the transfer of electrons from Ag to ZnO. The electron-rich  $Zn^+$  species in ZnO was speculated to serve as active sites to adsorb and activate  $N_2$  molecules, thereby promoting  $N_2$  photofixation.

**Key words:** silver; surface plasmon resonance; Schottky barrier;  $N_2$  photofixation; plasmonic catalysis

**CLC number:** O643.36; O644 **Document code:** A **Article ID:** 1004-0676(2021)04-0047-08

## Ag/ZnO 复合材料在氮气光固定中的应用：构造肖特基势垒以实现有效的电荷载流子分离

肖宇, 欧阳宇欣, 辛月, 王梁炳\*

(中南大学 材料科学与工程学院 粉末冶金国家重点实验室, 长沙 410083)

**摘要:** 将氮气( $N_2$ )光催化还原为氨( $NH_3$ )是一种可持续的能源生产方法。等离激元共振光催化剂能够通过表面等离激元共振效应实现太阳能的有效转化,也因此受到越来越广泛的关注。然而,热载流子往往会在催化固氮的过程中发生重新结合。本研究将具有等离激元共振效应的Ag纳米粒子与ZnO半导体复合(Ag/ZnO)并应用于氮气光固定。与ZnO相比,Ag/ZnO在氮气光固定的催化活性得到了提高,室温下氨生成速率达到  $120 \mu\text{mol} \cdot \text{g}_{\text{cat}}^{-1} \cdot \text{h}^{-1}$ 。进一步的机理研究表明在Ag纳米颗粒与ZnO的界面处形成了肖特基势垒,这大幅度促进了光生电子-空穴对的分离。Ag纳米粒子通过表面等离激元共振效应生成热载流子,所形成的肖特基势垒则促进了电子从Ag向ZnO转移。此外,ZnO中的富电子  $Zn^+$ 可能作为活性位点以吸附和活化氮气分子,从而促进氮气光固定的进行。

**关键词:** 银; 表面等离激元共振; 肖特基势垒; 氮气光固定; 等离激元共振催化

Nitrogen ( $N_2$ ) photofixation with water to ammonia ( $NH_3$ ) is a sustainable approach for producing

收稿日期: 2021-03-04

基金项目: 国家自然科学基金(51801235, 51674303); 中南大学创新驱动项目(2018CX004); 中南大学启动资金项目(502045005)

第一作者: 肖宇, 男, 硕士研究生, 研究方向: 金属氧化物的光催化性能。E-mail: Xiaoyu2018@csu.edu.cn

\*通讯作者: 王梁炳, 男, 教授, 研究方向: 有色金属催化、小分子的高效活化转化。E-mail: wanglb@csu.edu.cn

valuable energy sources under mild conditions<sup>[1-2]</sup>. A wide range of catalysts have been designed and fabricated for N<sub>2</sub> photofixation<sup>[3-10]</sup>. With the capability to efficiently harvest and convert solar energy via SPR, plasmonic photocatalysts have attracted more and more attention recently<sup>[11-14]</sup>. SPR in plasmonic metals not only extends the adsorption range of light, but also generates hot electrons with enough energy for N<sub>2</sub> reduction during decaying<sup>[14-16]</sup>. For instance, light-harvesting plasmonic Au was coupled with catalytic Ru for N<sub>2</sub> photoreduction by Xiong and co-workers, and a NH<sub>3</sub> production rate of 101.4 μmol·g<sub>cat.</sub><sup>-1</sup>·h<sup>-1</sup> was obtained<sup>[9]</sup>. The plasmonic hot electrons along with the enhanced electric field induced by SPR effect of Au were considered to promote the dissociation of N<sub>2</sub> molecular and further the conversion of N<sub>2</sub> to NH<sub>3</sub>. Recently, we constructed porous CuFe bimetal for plasmonic N<sub>2</sub> photofixation, where Cu frameworks generated hot electrons by SPR, while surface Fe atoms functioned as the active sites to adsorb and activate N<sub>2</sub> molecules<sup>[10]</sup>. Though some progress has been made in plasmon-assisted N<sub>2</sub> photofixation, the photo-generated charge carriers *via* SPR often suffer from severe recombination during photocatalysis, resulting in low hot electrons concentration and low N<sub>2</sub> reduction rate. Fortunately, to integrate plasmonic metals with appropriate semiconductors is a promising approach for improving the efficiency of charge carriers separation through forming Schottky barrier at the interface<sup>[17-21]</sup>. Generally, Schottky barrier is formed at the interface through the downward bending of the conduction band of the semiconductor, so that the Fermi levels in the metal and the semiconductor are aligned<sup>[18]</sup>. The Schottky barrier filters energetic electrons to pass through the interface and inhibits the recombination of plasmonic charge carriers, leading to the effective separation of electron-hole pairs for N<sub>2</sub> photofixation<sup>[19-20]</sup>.

Herein, we successfully synthesized Ag/ZnO photocatalyst by depositing plasmonic Ag nanoparticles onto ZnO. Without adding any sacrificial agent, Ag/ZnO photocatalyst achieved a NH<sub>3</sub> production rate of 120 μmol·g<sub>cat.</sub><sup>-1</sup>·h<sup>-1</sup>, which is about 2.1-fold higher than ZnO. NH<sub>3</sub> production rate retained

more than 90% of initial activity after five successive reaction cycles, indicating the outstanding stability of Ag/ZnO. Mechanism studies demonstrated that the Schottky barrier was formed in Ag/ZnO photocatalyst, promoting the efficiency of charge separation. In situ XPS and XAS measurement revealed that Ag NPs generated hot charge carriers via SPR effect, which then moved to ZnO under the photocatalytic condition. We further detected the electron-rich Zn<sup>+</sup> species in Ag/ZnO photocatalyst by ESR measurement, which was speculated to serve as active sites to adsorb and activate N<sub>2</sub> molecule. As a result, the Schottky barrier facilitated the transfer of electrons from Ag NPs to ZnO and the Zn<sup>+</sup> species enhanced the N<sub>2</sub> photofixation.

## 1 Experiments

### 1.1 Materials

Zinc nitrate hexahydrate (Zn(NO<sub>3</sub>)<sub>2</sub>·6H<sub>2</sub>O), 2-methylimidazole, silver nitrate (AgNO<sub>3</sub>), methane sulfonic acid (CH<sub>3</sub>SO<sub>3</sub>H), methanol (CH<sub>3</sub>OH), and ethanol (C<sub>2</sub>H<sub>5</sub>OH) were purchased from Sinopharm Chemical Reagent Co., Ltd. High purity nitrogen (N<sub>2</sub>, ≥99.999%) used in this work was gained from Saizongtezhong gas Co. LTD in Changsha. All solvents and chemicals were in analytical grade. All aqueous solutions were prepared using deionized water with a resistivity of 18.2 MΩ·cm<sup>-1</sup>.

### 1.2 Synthesis of ZnO and Ag/ZnO

Zeolitic imidazolate framework-8 (ZIF-8) was firstly prepared for the synthesis of ZnO. 3.7 g of Zn(NO<sub>3</sub>)<sub>2</sub>·6H<sub>2</sub>O and 4.1 g of 2-methylimidazole were added into 500 mL of methanol at room temperature. After 24 h, ZIF-8 was obtained by collecting the precipitation in the suspension solution. 100 mg of ZIF-8 was then heated to 500°C in a muffle furnace and kept it at 500°C for 3 h, the resulted powder was ZnO. The synthesized ZnO powder was immersed in a solution containing 1.07 mg of AgNO<sub>3</sub>, 35 mL of methanol, and 35 mL of ethanol, followed by stirring them at room temperature for 6 h. The resulted mixture was then transferred to a Teflon-lined stainless-steel autoclave and kept it at 120°C for 8 h. The Ag/ZnO composite was finally acquired via suction filtration with copious

deionized water and dried at 40°C under vacuum for 2 hours.

### 1.3 Photocatalytic experiments

Catalytic tests for N<sub>2</sub> photofixation were carried out in a 100-mL glass reactor. For a typical reaction, 10 mg of photocatalysts and 20 mL of deionized water were added into a 100-mL photo-reactor, followed by bubbling N<sub>2</sub> at a flow rate of ca. 30 mL·min<sup>-1</sup> for 30 min. Subsequently, the suspension was irradiated under vigorous stirring by a Xenon lamp (Perfectlight PLS-SXE300) under full-spectrum with an intensity of 250 mW·cm<sup>-2</sup>. The generated NH<sub>3</sub> was analyzed via an ion chromatograph method. To test the recycling of Ag/ZnO, the first measurement was conducted as described above, and the used catalysts were then washed and collected by centrifugation with deionized water for the next catalytic cycle.

### 1.4 Detection of NH<sub>3</sub>

The concentration of NH<sub>3</sub> was determined by an ion chromatograph method. 4.5 mmol·L<sup>-1</sup> of methane sulfonic acid was used as the eluent solution with a flow rate of 1 mL·min<sup>-1</sup>. The column temperature and self-regenerating suppressor current were kept as 35°C and 75 mA, respectively. 25 μL of quantitative injection loop was injected into the column. The retention time of NH<sub>4</sub><sup>+</sup> cations was at ~4.0 min. A standard curve of peak areas vs the concentrations of standard solution was firstly plotted. To determine the generated NH<sub>3</sub>, 25 μL of reaction solution was analyzed via this method. Based on the peak areas and standard curve, the concentration of NH<sub>3</sub> was obtained. It was worth mentioning that the acid in eluent solution guaranteed the generated NH<sub>3</sub> completely transformed to NH<sub>4</sub><sup>+</sup> which can be determined by ion chromatograph.

### 1.5 *In situ* XPS measurements

*In situ* XPS measurements were performed at the photoemission end-station and beamline BL10B in the National Synchrotron Radiation Laboratory (NSRL) in Hefei, China. The beamline is connected to a bending magnet and covers photon energies from 100 to 1,000 eV with a resolving power ( $E/\Delta E$ ) better than 1,000, and the photon flux was  $1 \times 10^{10}$  photons per s. The end-station is composed of four chambers: an analysis chamber, a preparation chamber, a load-lock chamber,

and a high-pressure reactor. The analysis chamber, with a base pressure of  $<2 \times 10^{-10}$  torr, is connected to the beamline with a VG Scienta R3000 electron energy analyser and a twin anode X-ray source. In addition, the analysis chamber is equipped with a window to allow the irradiation of light during the measurement of XPS spectra. In this work, the *in situ* XPS measurements of Ag/ZnO were conducted with/without light irradiation, which were named as “Ag/ZnO” and “Ag/ZnO+light”, respectively.

### 1.6 *In situ* Zn L-edge XAS measurements.

*In situ* Zn L-edge measurements were performed at the photoemission end-station and beamline BL10B in the National Synchrotron Radiation Laboratory (NSRL) in Hefei, China. The beamline and end-station are the same as those described in Section 2.5. The high-pressure reactor contains a reaction cell where the samples can be treated with different gases up to 20 bar and simultaneously heated up to 650°C. After the sample treatment, the reactor can be pumped down to  $<10^{-8}$  torr for sample transfer. In this work, the *in situ* Zn L-edge measurements of Ag/ZnO were conducted with/without light irradiation, which were named as “Ag/ZnO” and “Ag/ZnO+light”, respectively.

### 1.7 Instrumentations

TEM images were collected on a JEOL ARM-200F field-emission transmission electron microscope operating at 200 kV accelerating voltage. X-ray diffraction (XRD) patterns were recorded by using a Philips X'Pert Pro Super diffractometer with Cu-K $\alpha$  radiation ( $\lambda = 1.54178 \text{ \AA}$ ), and the  $2\theta$  range is from 10 to 80°. X-ray photoemission spectroscopy and X-ray absorption spectroscopy experiments were conducted at the Catalysis and Surface Science End-station connected to the BL10B beamline in NSRL in Hefei, China. UV-Vis tests were conducted on a TU-1901 at room temperature. ESR spectra were taken on JEOL JES-FA200 ESR spectrometer at 298 K.

## 2 Results and discussions

### 2.1 Characterization of materials

The morphology and structure of the samples were characterized by TEM as shown in Fig.1.

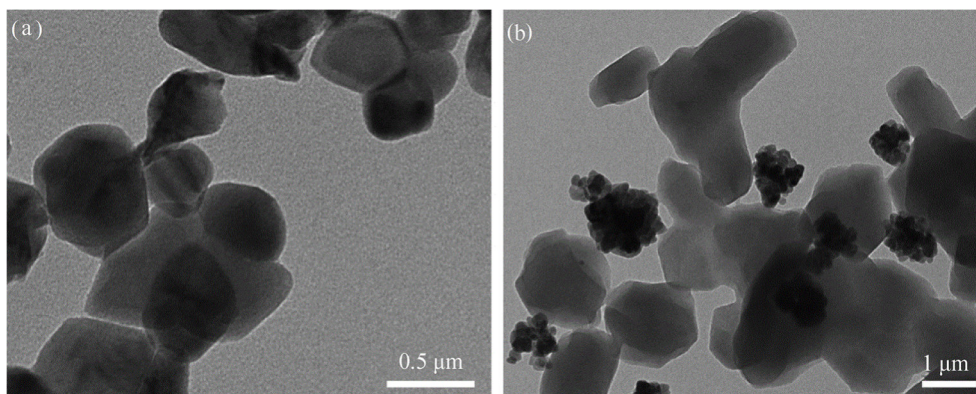


Fig.1 TEM images of ZnO (a) and Ag/ZnO (b)

图 1 ZnO(a)和 Ag/ZnO (b)的透射电子显微镜图像

Fig.1(a) shows the microstructure of ZnO prepared via heating ZIF-8 to 500°C in a muffle furnace. It can be seen from Fig.1(a) that the average particle size of ZnO was ~500 nm. Fig.1(b) illustrated the TEM image of Ag/ZnO formed through a hydrothermal process by dispersing ZnO powders into alcoholic solution of Ag ions. It is clear that Ag NPs besides ZnO.

XRD analysis was further adopted to characterize the composition of the as-prepared powders as shown in Fig.2.

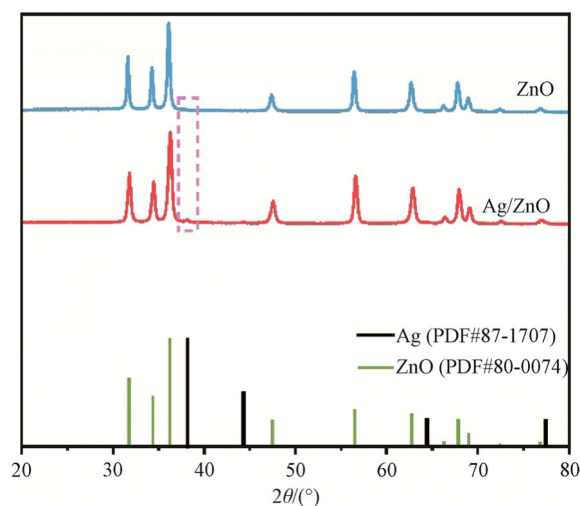


Fig.2 XRD patterns of ZnO and Ag/ZnO

图 2 ZnO 和 Ag/ZnO 的 X 射线衍射图谱

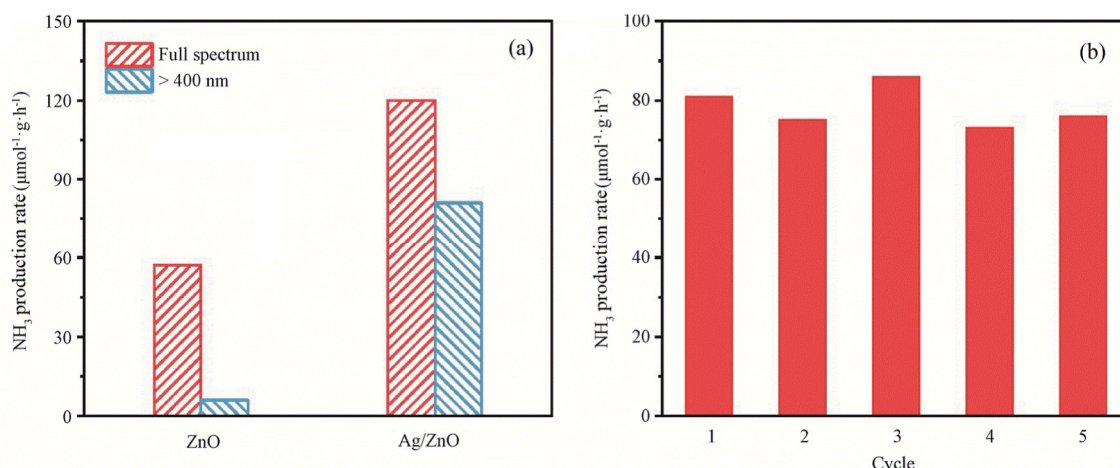
Fig.2 showed the XRD patterns of as-prepared catalysts. The XRD pattern of obtained ZnO matches the ZnO phase reference (PDF#80-0074). As to Ag/ZnO, there is an additional peak at 38.1° which was

related to the reference pattern of Ag (PDF#87-1707) phase. The XRD results agreed with the analysis of TEM images, manifesting the co-existence of ZnO and Ag NPs in Ag/ZnO.

## 2.2 Photocatalytic performance

The photocatalytic performance of obtained catalysts was evaluated through N<sub>2</sub> photofixation reaction. Each reaction cycle was conducted in 20 mL of deionized water purged with pure N<sub>2</sub> after adding 10 mg of catalysts at room temperature. The generated NH<sub>3</sub> was measured through an ion chromatography method. No NH<sub>3</sub> was detected for blank experiments.

As shown in Fig.3(a), the NH<sub>3</sub> production rates over ZnO were 57 and 6 μmol·g<sub>cat</sub><sup>-1</sup>·h<sup>-1</sup> under full-spectrum light irradiation (320~780 nm, 250 mW/cm<sup>2</sup>) and visible light (400~780 nm, 200 mW/cm<sup>2</sup>), respectively. After depositing Ag NPs with SPR on ZnO, the NH<sub>3</sub> production rate was up to 120 μmol·g<sub>cat</sub><sup>-1</sup>·h<sup>-1</sup> under the same full-spectrum range. Meanwhile, Ag/ZnO showed higher photocatalytic activity under visible light with 81 μmol·g<sub>cat</sub><sup>-1</sup>·h<sup>-1</sup> of NH<sub>3</sub> production rate as shown in Fig.3(a). To further corroborate the superior property of Ag/ZnO in photocatalytic reduction of N<sub>2</sub>, Ag/ZnO was recycled to test its stability as shown in Fig.3(b). More than 90% of initial activity was retained in N<sub>2</sub> photofixation after five cycles, indicating the remarkable catalytic stability of Ag/ZnO. As a result, Ag/ZnO exhibited remarkable activity and endurance towards the photocatalytic reduction of N<sub>2</sub>.



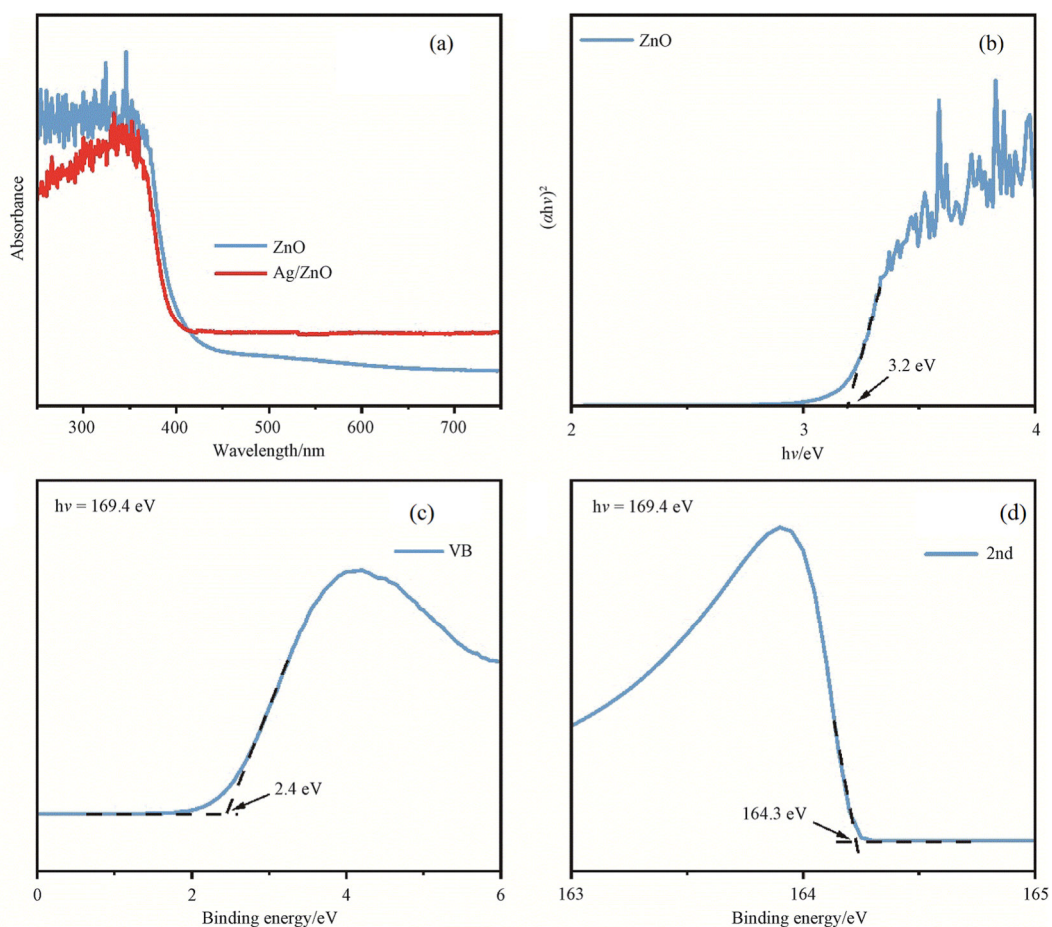
**Fig.3 (a).** The NH<sub>3</sub> production rates catalyzed by ZnO and Ag/ZnO under full-spectrum and filtered light irradiation of Xenon lamp; **(b).** NH<sub>3</sub> production rate of Ag/ZnO catalysts at five successive reaction cycles

图 3 (a). 全光谱和可见光照射下 ZnO 和 Ag/ZnO 的氨生成速率; (b). 五轮连续反应过程中 Ag/ZnO 的氨生成速率

### 2.3 Photocatalytic mechanisms

To explore the origin of the excellent catalytic performance of Ag/ZnO in N<sub>2</sub> photofixation, the

catalytic mechanism was investigated in details as shown in Fig.4.



**Fig.4 (a).** Diffuse reflectance UV-Vis spectra of the obtained samples of ZnO and Ag/ZnO;

**(b).** Transformed K-M function for ZnO; **(c).** Valence band spectrum; **(d).** Secondary electron cutoff of ZnO

图 4 (a). ZnO 和 Ag/ZnO 的紫外-可见漫反射光谱; (b). ZnO 的 K-M 变换函数; (c). ZnO 的价带谱; (d). 二次电子截止边

Fig.4(a) displayed the diffuse reflectance ultraviolet-visible (UV-Vis) spectra of ZnO and Ag/ZnO. The absorption spectrum of Ag/ZnO was similar to that of ZnO with a steep absorption increase at 350~400 nm. However, the adsorption of Ag/ZnO was obviously enhanced in visible region owing to the SPR of metallic Ag. As shown in Fig.4(b), the calculated band gap of ZnO was 3.2 eV via a transformed Kubelka-Munk (K-M) plot. In addition, synchrotron radiation photoemission spectroscopy (SRPES) was conducted with a photon energy of 169.4 eV. Fig.4(c) displayed the valence band (VB) spectra of ZnO. It can be seen from Fig.4(c) that the maximum VB of ZnO was 2.4 eV which is below the Fermi level ( $E_f$ ) secondary electron cutoff was performed to confirm the position of  $E_f$  versus vacuum level ( $E_{vac}$ ), where the value of work function ( $\Phi$ ) for ZnO was 5.1 eV (Fig.4(d)). Thus, the calculated value of maximum VB for ZnO was 7.5 eV versus  $E_{vac}$ . As normal hydrogen electrode (NHE) was 4.5 eV versus  $E_{vac}$ <sup>[22]</sup>, the values of maximum VB and  $E_f$  for ZnO were determined to be 3.0 and 0.6 eV versus NHE, respectively. Furthermore, considering the 3.2 eV of band gap for ZnO, the calculated conduction band (CB) of ZnO was -0.2 eV versus NHE. The  $E_f$  versus NHE was generally 1.0 eV for metal Ag.

Based on above analysis, the corresponding electronic band structure versus NHE of Ag/ZnO was depicted in Fig.5.

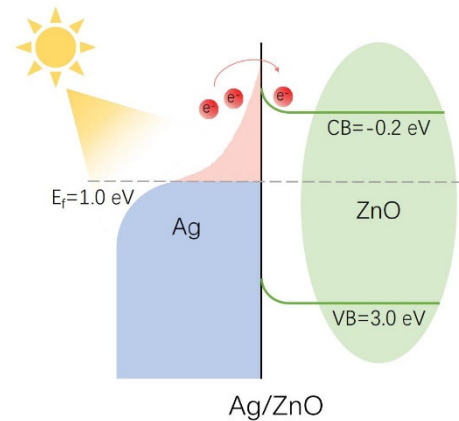


Fig.5 Schematic illustration of the band structure of Ag/ZnO

图 5 Ag/ZnO 的能带结构示意图

The contact between metallic Ag and ZnO semiconductor equalized the  $E_f$  values of the two materials, creating Schottky barrier at the interface between Ag nanoparticle and ZnO. Ag NPs generated hot electrons by SPR effect under illumination, while the formed Schottky barrier facilitated the transfer of electrons from Ag NPs to the CB of ZnO, directly boosting the separation of electron-hole pairs for further  $N_2$  reduction process (Fig.5).

A series of *in situ* experiments were further conducted to reveal the electronic dynamics of Ag/ZnO during  $N_2$  photofixation, as shown in Fig.6.

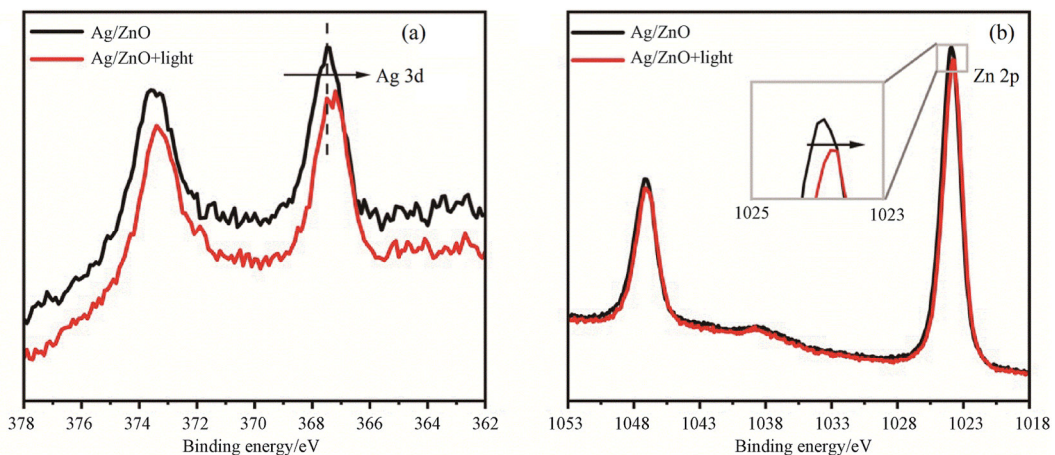


Fig.6 In situ XPS spectra of Ag 3d (a) and Zn 2p (b) for Ag/ZnO measured with/without light irradiation

图 6 有光照及无光照时 Ag/ZnO 的 Ag 3d(a)和 Zn 2p(b)原位 X 射线光电子能谱

Fig.6 displayed the *in situ* X-ray photoelectron spectroscopy (XPS) spectra of Ag/ZnO. As displayed in the Ag 3*d* XPS spectra, the binding energies of Ag 3*d*<sub>5/2</sub> and 3*d*<sub>3/2</sub> for Ag/ZnO were fitted at 367.5 and 373.6 eV under dark, respectively, indicating a metallic Ag state in Ag/ZnO (Fig.6(a))<sup>[23]</sup>. In the XPS spectra of Zn 2*p*, the peaks centered at 1023.9 and 1047.1 eV were assigned to Zn 2*p*<sub>3/2</sub> and 2*p*<sub>1/2</sub> signals, respectively, proving that the Zn species were mainly in oxidation states as shown in Fig.6(b)<sup>[24-26]</sup>. Accordingly, the XPS results in dark disclosed that Ag was presented in metal state in Ag/ZnO whereas Zn existed in oxidized state, consistent to the XRD results. Furthermore, when Ag/ZnO was under irradiation, both Ag 3*d* and Zn 2*p* XPS spectra moved towards the lower binding energy direction, indicative of the electron transfer from Ag to Zn under the irradiation of light (Fig.6(a) and Fig.6(b))<sup>[27-28]</sup>.

In order to confirm the electronic properties, *in situ* Zn L-edge X-ray absorption spectroscopy (XAS) was also analyzed, as shown in Fig.7. The lower peak intensity of the spectrum of Zn L-edge XAS under illumination was attributed to the decrease of the valence state of Zn species, which further demonstrated electrons accumulation in Zn species under light irradiation (Fig.7)<sup>[29]</sup>. As a result, the formation of Schottky barrier promoted the separation of photo-excited electron-hole pairs, leading to the electron transfer from Ag NPs to ZnO.

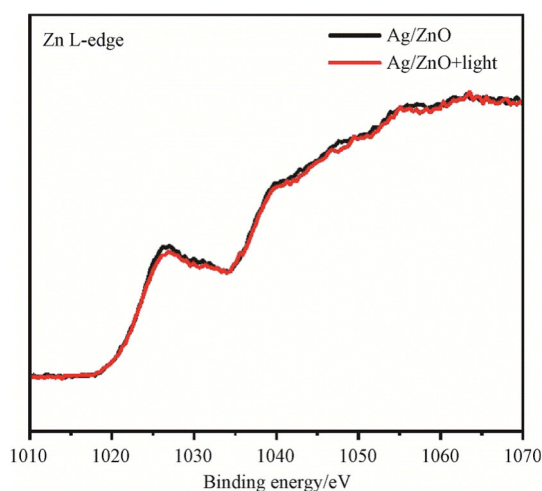


Fig.7 *In situ* Zn L-edge XAS spectra for Ag/ZnO under dark and light

图7 光照及黑暗时 Ag/ZnO 的原位 Zn L-边 X 射线吸收光谱

Electron spin resonance (ESR) spectroscopy was conducted (Fig.8) for further characterization. As depicted in Fig.8, an ESR signal with  $g=1.999$  assigned to the oxygen vacancy was observed for ZnO<sup>[6]</sup>. More importantly, an obvious ESR signal with  $g=1.960$  ascribed to Zn<sup>+</sup> cations (3*d*<sup>10</sup>4*s*<sup>1</sup>) appeared for both ZnO and Ag/ZnO, suggesting that Zn<sup>+</sup> species was presented on the ZnO and Ag/ZnO<sup>[30]</sup>. Thus, the electrons were speculated to prefer to be trapped by Zn<sup>+</sup> rather than delocalize over the lattice, which favored the efficient electron separation and transfer. The electron-rich Zn<sup>+</sup> was considered as active sites to chemisorb and activate N<sub>2</sub> molecules for the further transformation to NH<sub>3</sub>.

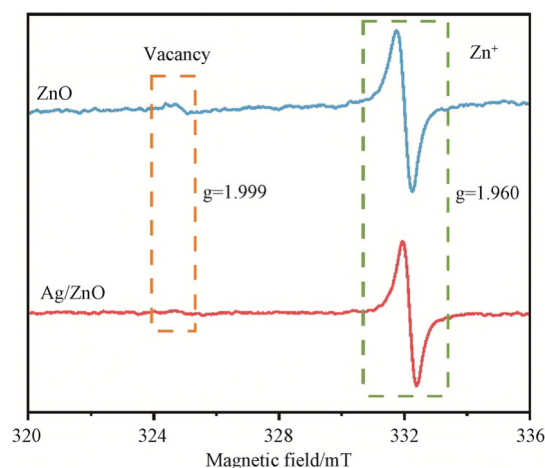


Fig.8 ESR signal of ZnO and Ag/ZnO

图8 ZnO 和 Ag/ZnO 的电子顺磁共振信号

### 3 Conclusions

In conclusion, we successfully deposited Ag NPs on ZnO containing Zn<sup>+</sup> and formed Schottky barrier. Ag/ZnO was witnessed to exhibit excellent activity and stability towards N<sub>2</sub> photofixation. The investigation of band structure for Ag/ZnO revealed the Schottky barrier generated at the interface between Ag and ZnO, which facilitated electrons transfer from Ag NPs to ZnO. Furthermore, the electron-rich Zn<sup>+</sup> species was considered as the active sites to chemisorb and activate N<sub>2</sub> molecules. This work not only promotes the separation efficiency of plasmonic charge carriers by constructing Schottky barrier, but also highlights a promising approach to prepare Zn<sup>+</sup> containing Ag/ZnO catalysts for long-term N<sub>2</sub> photoreduction.

**References:**

- [1] WANG S, ICHIHARA F, PANG H, et al. Nitrogen fixation reaction derived from nanostructured catalytic materials[J]. *Advanced Functional Materials*, 2018, 28(50): 1803309.
- [2] YANG J, GUO Y, LU W, et al. Emerging applications of plasmons in driving CO<sub>2</sub> reduction and N<sub>2</sub> fixation [J]. *Advanced Materials*, 2018, 30(48): 1802227.
- [3] HOU T, PENG H, XIN Y, et al. Fe single-atom catalyst for visible-light-driven photofixation of nitrogen sensitized by triphenylphosphine and sodium iodide [J]. *ACS catalysis*, 2020, 10(10): 5502-5510.
- [4] ZHAO Y, ZHAO Y, SUI R, et al. Tuning oxygen vacancies in ultrathin TiO<sub>2</sub> nanosheets to boost photocatalytic nitrogen fixation up to 700 nm [J]. *Advanced Materials*, 2019, 31(16): 1806482.
- [5] ZHANG N, JALIL A, WU D, et al. Refining defect states in W<sub>18</sub>O<sub>49</sub> by Mo doping: A strategy for tuning N<sub>2</sub> activation towards solar-driven nitrogen fixation [J]. *Journal of the American Chemical Society*, 2018, 140(30): 9434-9443.
- [6] HOU T, LI Q, ZHANG Y, et al. Near-infrared light-driven photofixation of nitrogen over Ti<sub>3</sub>C<sub>2</sub>Tx/TiO<sub>2</sub> hybrid structures with superior activity and stability [J]. *Applied Catalysis B: Environmental*, 2020, 273: 119072.
- [7] WANG W, ZHANG H, ZHANG S, et al. Potassium ion assisted regeneration of active cyano groups in carbon nitride nanoribbons: Visible light driven photocatalytic nitrogen reduction [J]. *Angewandte Chemie-International Edition*, 2019, 58(46): 16644-16650.
- [8] HOU T, XIAO Y, CUI P, et al. Operando oxygen vacancies for enhanced activity and stability toward nitrogen photofixation [J]. *Advanced Energy Materials*, 2019, 9(43): 1902319.
- [9] HU C, CHEN X, JIN J, et al. Surface plasmon enabling nitrogen fixation in pure water through a dissociative mechanism under mild conditions [J]. *Journal of the American Chemical Society*, 2019, 141(19): 7807-7814.
- [10] HOU T, CHEN L, XIN Y, et al. Porous CuFe for plasmon-assisted N<sub>2</sub> photofixation [J]. *ACS Energy Letters*, 2020, 5(7): 2444-2451.
- [11] ASLAM U, RAO V, CHAVEZ S, et al. Catalytic conversion of solar to chemical energy on plasmonic metal nanostructures [J]. *Nature Catalysis*, 2018, 1(9): 656-665.
- [12] ZHAN C, MOSKOVITS M, TIAN Z. Recent progress and prospects in plasmon-mediated chemical reaction [J]. *Matter*, 2020, 3(1): 42-56.
- [13] LI S, MIAO P, ZHANG Y, et al. Recent advances in plasmonic nanostructures for enhanced photocatalysis and electrocatalysis[J]. *Advanced Materials*, 2020, 33(6): 200086.
- [14] GELLÉ A, JIN T, GARZA L, et al. Applications of plasmon-enhanced nanocatalysis to organic transformations[J]. *Chemical Reviews*, 2020, 120(2): 986-1041.
- [15] ZHANG Y, HE S, GAO W, et al. Surface-plasmon-driven hot electron photochemistry [J]. *Chemical Reviews*, 2017, 118(6): 2927-2954.
- [16] LINIC S, ASLAM U, BOERIGTER C, et al. Photochemical transformations on plasmonic metal nanoparticles [J]. *Nature Materials*, 2015, 14(6): 567-576.
- [17] LINIC S, CHRISTOPHER P, INGRAM D. Plasmonic-metal nanostructures for efficient conversion of solar to chemical energy [J]. *Nature Materials*, 2011, 10(12): 911-921.
- [18] YU K, JIANG P, YUAN H, et al. Cu-based nanocrystals on ZnO for uranium photoreduction: Plasmon-assisted activity and entropy-driven stability [J]. *Applied Catalysis B: Environmental*, 2021, 288: 119978.
- [19] YANG J, GUO Y, JIANG R, et al. High-efficiency “working-in-tandem” nitrogen photofixation achieved by assembling plasmonic gold nanocrystals on ultrathin titania nanosheets [J]. *Journal of the American Chemical Society*, 2018, 140(27): 8497-8508.
- [20] XU X, LUO F, TANG W, et al. Enriching hot electrons via NIR-photon-excited plasmon in WS<sub>2</sub>@Cu hybrids for full-spectrum solar hydrogen evolution [J]. *Advanced Functional Materials*, 2018, 28(43): 1804055.
- [21] YANG Y, LUO M, ZHANG W, et al. Metal surface and interface energy electrocatalysis: Fundamentals, performance engineering, and opportunities [J]. *Chem*, 2018, 4(9): 2054-2083.
- [22] WANG L, HOU T, XIN Y, et al. Large-scale synthesis of porous Bi<sub>2</sub>O<sub>3</sub> with oxygen vacancies for efficient photodegradation of methylene blue [J]. *Chinese Journal of Chemical Physics*, 2020, 33(4): 500-506.
- [23] MUTHUCHAMY N, GOPALAN A, LEE K. A new facile strategy for higher loading of silver nanoparticles onto silica for efficient catalytic reduction of 4-nitrophenol [J]. *RSC Advances*. 2015, 5(93): 76170-76181.